Nucleic Acids Research, 2025, **53**, gkaf409
https://doi.org/10.1093/nar/gkaf409
Nucleic Acid Therapeutics

Modulation of *TTR* gene expression in the eye using modified siRNAs

Jiaxin Hu[1,†], Xin Gong[2,†], Jayanta Kundu[3], Dhrubajyoti Datta[3], Martin Egli[4], Muthiah Manoharan[3], V. Vinod Mootha[2,5,*,†], David R. Corey[1,*,†]

[1]Departments of Pharmacology and Biochemistry, UT Southwestern Medical Center, Dallas, TX 75390, United States
[2]Department of Ophthalmology, UT Southwestern Medical Center, Dallas, TX 75235, United States
[3]Alnylam Pharmaceuticals, Cambridge, MA 04142, United States
[4]Department of Biochemistry, School of Medicine, Vanderbilt University, Nashville, TN 37232, United States
[5]Eugene McDermott Center for Human Growth and Development, UT Southwestern Medical Center, Dallas, TX 75235, United States

[*]To whom correspondence should be addressed. Email: vinod.mootha@utsouthwestern.edu
Correspondence may also be addressed to David R. Corey. Email: David.corey@utsouthwestern.edu
[†]These authors contributed equally to this work.

Abstract

Small interfering RNAs (siRNAs) are a proven therapeutic approach for controlling gene expression in the liver. Expanding the clinical potential of RNA interference requires developing strategies to enhance delivery to extra-hepatic tissues. In this study, we examine inhibiting *transthyretin* (*TTR*) gene expression by siRNAs in the eye. Anti-*TTR* siRNAs have been developed as successful drugs to treat TTR amyloidosis. When administered systemically, anti-*TTR* siRNAs alleviate symptoms by blocking *TTR* expression in the liver. However, TTR amyloidosis also affects the eye, suggesting a need for reducing ocular *TTR* gene expression. Here, we demonstrate that pyrimidine C5- and 2′-O-linked lipid-modified siRNAs formulated in saline can inhibit *TTR* expression in the eye when administered locally by intravitreal injection. Modeling suggests that length and accessibility of the lipid chains contribute to *in vivo* silencing. GalNAc-modified siRNAs also inhibit *TTR* expression, albeit less potently. These data support lipid-modified siRNAs as an approach to treating the ocular consequences of TTR amyloidosis. Inhibition of *TTR* expression throughout the eye demonstrates that lipid–siRNA conjugates have the potential to be a versatile platform for ocular drug discovery.

Graphical abstract

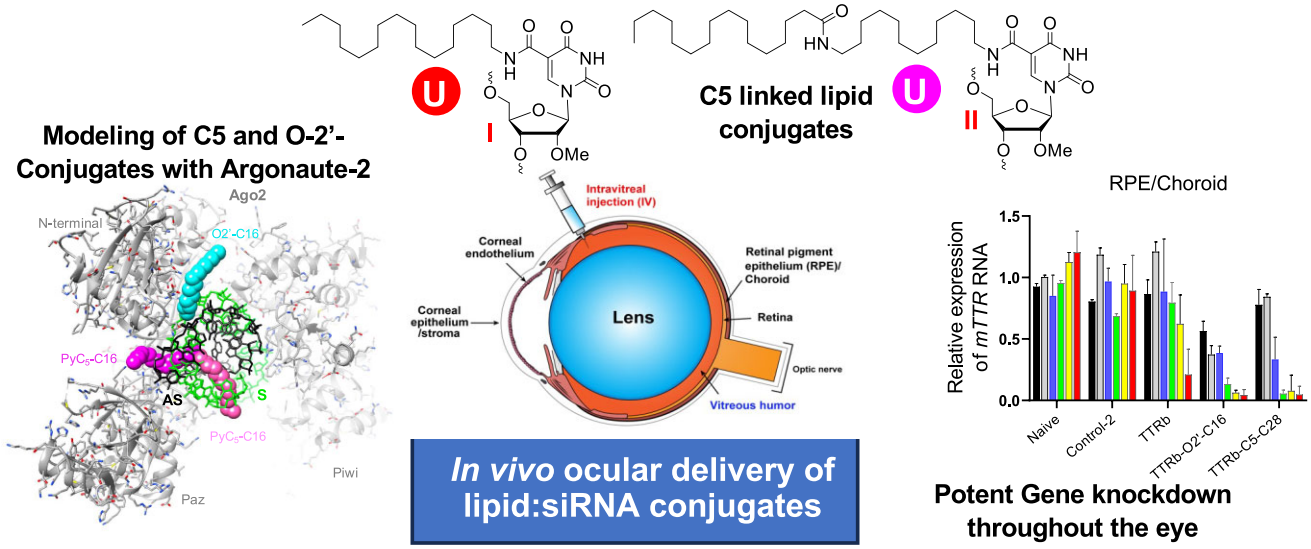

Introduction

Small interfering RNAs (siRNAs) that act through RNA interference (RNAi) are a powerful approach for drug discovery and development [1–3]. There are currently seven approved siRNA drugs, all silencing messenger RNA (mRNA) targets in the liver. These positive clinical results and associated pre-clinical results demonstrate the power of siRNAs to be versatile regulators of gene expression in hepatic tissue. The

Received: March 7, 2025. **Revised:** April 25, 2025. **Editorial Decision:** April 25, 2025. **Accepted:** May 1, 2025

open question is whether potent, selective, and clinically effective RNAi-mediated gene silencing can be extended to extra-hepatic tissues.

The success of siRNAs in the liver was enabled by the development of siRNA–GalNAc conjugates [4]. GalNAc conjugates target the asialoglycoprotein receptor (ASGPR) and dramatically increase the uptake of siRNAs in hepatocytes. Increased uptake leads to high potencies and ultimately contributes to greater success in the clinic. GalNAc conjugates are successful because of the large number of ASGPRs per cell and their quick recycling time. Unfortunately, the identification of receptors on other tissues that share the favorable properties of ASGPR has been slow, leading to interest in other modification strategies for optimizing siRNA delivery [1–3].

Strategies for extra-hepatic delivery have included cholesterol modification to improve skeletal delivery [5, 6], antibody conjugates that improve delivery to muscle [7], and divalent siRNAs that improve delivery to the central nervous system (CNS) [8]. Recently, lipid modification has been described as a general approach to delivery to extra-hepatic tissues, including CNS, lung, and eye [9].

The eye is a potentially advantageous organ for the delivery of nucleic acid drugs. The first approved nucleic acid drug, the antisense oligonucleotide (ASO) Vitravene (fomivirsen) in the 1990's was administered by (intravitreal; IVT) injection [10]. Two other approved nucleic acid aptamer drugs, macugen and izervay, were also administered by IVT injection [11]. Injection into the eye reduces the amount of drug needed and lowers the potential for systemic toxicities. IVT injection is one of the most common procedures in medicine and silencing gene expression in the eye might have therapeutic applications to many ocular diseases.

Our goal here was to explore the use of chemically modified lipid siRNA conjugates throughout varied parts of the eye. We chose *transthyretin* (*TTR*) as our target gene. *TTR* is the target of two approved siRNA drugs, one delivered using nanoparticles, patisiran [12] and the other as a GalNAc conjugate, vutrisiran [13]. Systemic administration is sufficient to target *TTR* in the liver and alleviate many of the devastating symptoms of TTR amyloidosis (ATTR), polyneuropathy [14, 15], and cardiomyopathy [16]. ATTR can also lead to loss of vision by causing vitreous opacities, glaucoma, keratoconjunctivitis sicca (dry eye), and neurotrophic corneal disease [17–20]. Systemic administration of the approved siRNA drugs does not treat ocular systems, presumably because of the barriers between the bloodstream and intraocular tissue [21]. *TTR* expression, therefore, serves as a model gene for evaluating the action of siRNAs in the eye.

While 90% of TTR protein is synthesized by the liver, TTR is also produced by the choroid plexus in the brain and retinal pigment epithelial (RPE) cells in the eye [22]. Progression of ocular involvement of ATTR is observed in patients even after liver transplantation (a surgical treatment for ATTR), despite the inability of plasma TTR to cross the blood–retina barrier [21]. This finding suggests that ocular symptoms of ATTR are due to the local production of mutant TTR in the RPE.

Intraocular amyloid deposits have been detected in tissue structures across the eye including the corneal endothelium, trabecular meshwork, iris epithelium, ciliary pigment epithelium, lens capsule, vitreous, RPE, and retinal nerve fibers [18, 20, 23]. ATTR can result in deposits at the inner pupillary margin resulting in its scalloped appearance and an altered pupillary light reflex [18]. The reported prevalence of vitreous opacities in ATTR ranges from 5.4 to 35% [17]. The collagen in the vitreous acts as a scaffold for the accumulation of amyloid that can result in a visual complaint of floaters and progressive loss of visual acuity.

The current surgical treatment to restore vision is vitrectomy but the opacities may recur. Approximately 18% of patients can also develop a chronic open angle glaucoma due to amyloid deposition in the trabecular meshwork and/or increased episcleral venous pressure [17]. The glaucoma may be refractory to topical glaucoma medications and require surgery. These deficiencies in current treatments suggest a need for reduction of ocular TTR gene expression.

Here, we show that lipid-modified siRNAs (Fig. 1 and Supplementary Table S1) are potent inhibitors of *TTR* expression throughout diverse tissue in the eye, suggesting that lipidated siRNAs may be a broadly useful starting point for ocular drug discovery beyond their potential use limiting *TTR* expression. Molecular modeling suggests that the length of the lipid chain and its point of attachment are critical variables governing activity. Specific to ATTR, GalNAc-modified siRNAs are less efficacious but also inhibit *TTR* expression, suggesting that drugs that are already approved for systemic administration might be candidates for IVT administration to patients at risk for ocular sequelae from ATTR. Potent inhibition by multiple lipidated anti-*TTR* siRNAs suggests that lipid conjugates can also provide strategy for treating the ocular findings of ATTR.

Materials and methods

General synthetic protocols

Thin-layer chromatography (TLC) was performed on Merck silica gel 60 plates coated with F254. Compounds were visualized under ultraviolet (UV) light (254 nm) or after spraying with the p-anisaldehyde staining solution followed by heating. Flash column chromatography was performed using a Teledyne ISCO Combi Flash system with pre-packed RediSep Teledyne ISCO silica gel cartridges. All moisture-sensitive reactions were carried out under anhydrous conditions using dry glassware, anhydrous solvents, and argon atmosphere. All commercially available reagents and solvents were purchased from Sigma–Aldrich unless otherwise stated and were used as received. ^{1}H Nuclear magnetic resonance (NMR) spectra were recorded at 600 MHz (Supplementary Fig. S4). ^{13}C NMR spectra were recorded at 151 MHz. ^{31}P NMR spectra were recorded at 243 MHz. Chemical shifts are given in ppm referenced to the solvent residual peak ($CDCl_3$ – ^{1}H: δ at 7.26 ppm and ^{13}C δ at 77.2 ppm). Coupling constants are given in Hertz. Signal splitting patterns are described as singlet (s), doublet (d), triplet (t), or multiplet (m).

1-((2R,3R,4R,5R)-5-((bis(4-methoxyphenyl)(phenyl)methoxy)methyl)-4-hydroxy-3-methoxytetrahydrofuran-2-yl)-*N*-hexadecyl-2,4-dioxo-1,2,3,4-tetrahydropyrimidine-5-carboxamide **1**

To a clear solution of 2,2,2-trifluoroethyl 1-((2R,3R,4R,5R)-5-((bis(4-methoxyphenyl)(phenyl)methoxy)methyl)-4-hydroxy-3-methoxytetrahydrofuran-2-yl)-2,4-dioxo-1,2,3,4-tetrahydropyrimidine-5-carboxylate (C5-TFE ester) [24] (1.0 g, 1.46 mmol) in acetonitrile (ACN) (10 ml) was added 1-aminohexadecane (1.06 g, 4.38 mmol) and the reaction

A

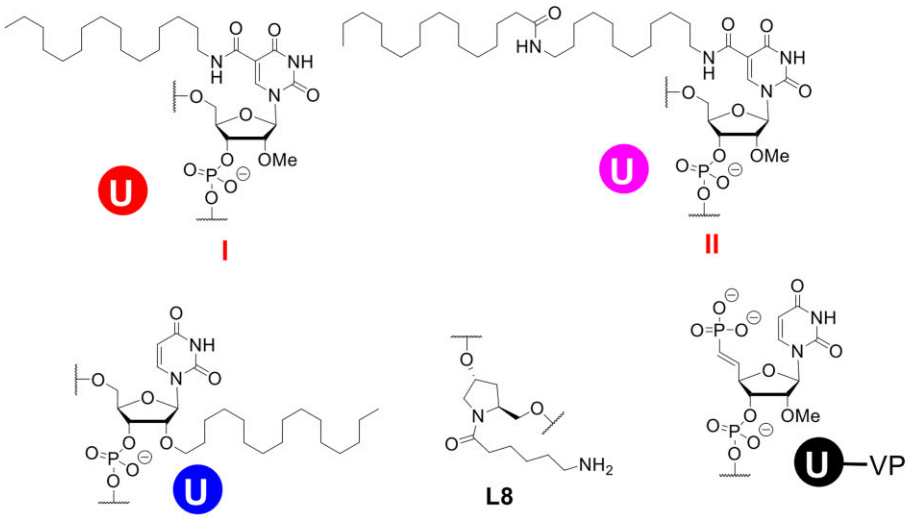

B

ID	Bead diagram (sense at top from 5′ to 3′)[a]	Description
TTRa	AACAGUGUUCUUGCUCUAUAA—L8 UUUUGUCACAAGAACGAGAUAUU—VP	L8 (26) control 1 with no lipid
TTRa-C5-C16	AACAGUGUUCUUGCUCUAUAA—L8 UUUUGUCACAAGAACGAGAUAUU—VP	C5-functionalized-U containing C16 alkyl chain
TTRa-GalNAc	AACAGUGUUCUUGCUCUAUAA—GalNAc UUUUGUCACAAGAACGAGAUAUU—VP	With GalNAc (4,27)
TTRb	AACAGUGUUCUUGCUCUAUAA—L8 UUUUGUCACAAGAACGAGAUAUU—VP	L8 control 2 with no lipid
TTRb-O2′-C16	AACAGUGUUCUUGCUCUAUAA UUUUGUCACAAGAACGAGAUAUU—VP	With 2′-O16 lipid (9)
TTRb-C5-C28	AACAGUGUUCUUGCUCUAUAA—L8 UUUUGUCACAAGAACGAGAUAUU—VP	C5-functionalized-U containing C28 alkyl chain
Control-1	CAUUUUAAUCCUCACUCUAAA GAGUAAAAUUAGGAGUGAGAUUU—VP	Negative control C5-functionalized-U containing C16 alkyl chain
Control-2	CAUUUUAAUCCUCACUCUAAA—L8 GAGUAAAAUUAGGAGUGAGAUUU—VP	Negative control C5-functionalized-U containing C28 alkyl chain

Figure 1. (**A**) Structural representation of C5-lipid, L8 linker, and vinyl phosphonate (VP) modifications used in lipid-modified siRNAs. (**B**) Duplexes used in these studies. 2′-Fluoro (2′-F) and 2′-*O*-methyl (2′-OMe) nucleotides are indicated in green and black, respectively. Phosphorothioate (PS) linkages are indicated by orange vertical lines. Uridines linked to lipid at the C5 position are red, and uridines linked to lipid at the 2′-O position are blue.

mixture was allowed to stir at 45°C for 12 h. TLC showed that starting material was almost consumed (90%). The volatile matter of the reaction mixture was concentrated under high vacuum pump to get the crude compound which was purified by silica gel column chromatography eluting with 30%–50% EtOAc in hexane to afford **1** (1.05 g, 88% yield) as yellowish white solid. ^{1}H NMR (600 MHz, $CDCl_3$) δ 8.56 – 8.44 (m, 2H), 7.47 – 7.43 (m, 2H), 7.38 – 7.33 (m, 4H), 7.29 – 7.25 (m, 2H), 7.20 – 7.16 (m, 1H), 6.87 – 6.78 (m, 4H), 5.88 (s, 1H), 4.11 (d, J = 6.2 Hz, 1H), 4.05 – 4.01 (m, 1H), 3.87 (dd, J = 5.8, 3.1 Hz, 1H), 3.78 (s, 6H), 3.53 (s, 3H), 3.45 (t, J = 4.7 Hz, 2H), 3.37 – 3.32 (m, 2H), 1.55 (d, J = 7.4 Hz, 2H), 1.25 (s, 26H), 0.88 (t, J = 7.0 Hz, 3H) ppm. ^{13}C NMR (151 MHz, $CDCl_3$) δ 160.9, 160.9, 158.5, 149.2, 146.2, 144.7, 135.8, 135.8, 130.1, 130.1, 128.1, 127.9, 126.8, 113.2, 113.2, 107.0, 89.2, 86.7, 83.6, 82.8, 69.8, 63.3, 58.9, 55.2, 39.5, 31.9, 29.7, 29.7, 29.7, 29.7, 29.6, 29.5, 29.4, 29.4, 27.1, 22.7, 14.1 ppm.

(2R,3R,4R,5R)-2-((bis(4-methoxyphenyl)(phenyl)methoxy)methyl)-5-(5-(hexadecylcarbamoyl)-2,4-dioxo-3,4-dihydropyrimidin-1(2H)-yl)-4-methoxytetrahydrofuran-3-yl (2-cyanoethyl) diisopropylphosphoramidite **2**

To a clear solution of **1** (1.02 g, 1.25 mmol) in anhydrous dichloromethane (DCM) (15 ml) were added *N*-methylimidazole (NMI) (204.95 mg, 2.50 mmol, 198.98 µl) and *N*,*N*-diisopropylethylamine (DIPEA) (806.54 mg, 6.24

mmol, 1.09 ml). After stirring for 5 min, 2-cyanoethyl-*N*,*N*-diisopropylchlorophosphoramidite (590.8 mg, 2.50 mmol, 556.8 µl) was added and the reaction mixture was allowed to stir for 0.33 h. TLC showed complete consumption of the starting material. The reaction mixture was quenched with aq $NaHCO_3$, diluted with anhydrous DCM, and washed with water and brine. The organic layer was dried over Na_2SO_4, filtered, and concentrated to get the crude product which was purified by silica gel column chromatography eluting with 40%–60% EtOAc-hexane to afford **2** (1.06 g, 84% yield) as a white solid. ^{1}H NMR (600 MHz, $CDCl_3$) δ 8.59 – 8.42 (m, 2H), 7.46 (ddt, *J* = 13.8, 6.5, 1.4 Hz, 2H), 7.40 – 7.32 (m, 4H), 7.30 – 7.25 (m, 2H), 7.19 (qd, *J* = 6.1, 1.3 Hz, 1H), 6.91 – 6.77 (m, 4H), 5.96 – 5.86 (m, 1H), 4.30 – 4.17 (m, 2H), 4.02 – 3.93 (m, 1H), 3.79 (d, *J* = 4.4 Hz, 6H), 3.68 – 3.50 (m, 3H), 3.44 (d, *J* = 10.8 Hz, 3H), 3.36 (ddd, *J* = 14.8, 5.5, 2.7 Hz, 4H), 2.67 – 2.29 (m, 2H), 1.56 (q, *J* = 6.6 Hz, 2H), 1.25 (s, 24H), 1.15 (dd, *J* = 6.8, 5.3 Hz, 9H), 1.03 (d, *J* = 6.8 Hz, 4H), 0.88 (t, *J* = 7.0 Hz, 3H) ppm. ^{13}C NMR (151 MHz, $CDCl_3$) δ 162.4, 160.9, 158.5, 149.2, 146.4, 146.3, 144.6, 135.8, 135.7, 135.6, 130.2, 130.2, 130.1, 128.2, 128.1, 127.9, 126.8, 117.8, 113.2, 113.2, 113.2, 113.2, 107.0, 106.9, 88.9, 88.8, 86.7, 86.7, 83.5, 83.5, 83.4, 83.3, 82.2, 82.1, 81.4, 81.4, 71.0, 70.9, 70.5, 70.4, 63.2, 62.8, 58.7, 58.7, 58.6, 58.3, 58.3, 57.9, 57.8, 55.2, 55.2, 43.4, 43.3, 43.2, 43.1, 39.5, 39.4, 31.9, 29.7, 29.7, 29.7, 29.6, 29.6, 29.5, 29.5, 29.4, 27.1, 24.6, 24.6, 24.6, 24.5, 24.5, 22.7, 20.4, 20.3, 20.2, 20.1, 14.1 ppm. ^{31}P NMR (243 MHz, $CDCl_3$) δ 150.95, 150.20 ppm.

N-(12-aminododecyl)-1-((2R,3R,4R,5R)-5-((bis(4-methoxyphenyl)(phenyl)methoxy)methyl)-4-hydroxy-3-methoxytetrahydrofuran-2-yl)-2,4-dioxo-1,2,3,4-tetrahydropyrimidine-5-carboxamide **3**

To a clear solution of C5-TFE ester [24] (1 g, 1.46 mmol) in anhydrous ACN (15 ml) was added dodecanediamine (291.80 mg, 1.46 mmol) and the reaction mixture was heated at 50°C for 12 h. TLC showed complete consumption of the starting material. The volatile matter of the reaction mixture was concentrated under high vacuum pump to get the crude product which was purified by silica gel column chromatography eluting with 0%–30% MeOH-DCM to afford **3** (922 mg, 80% yield) as white foam. ^{1}H NMR (600 MHz, $CDCl_3$) δ 8.70 (t, *J* = 5.6 Hz, 1H), 8.47 (s, 1H), 7.48 – 7.42 (m, 2H), 7.37 – 7.32 (m, 4H), 7.28 – 7.23 (m, 3H), 7.21 – 7.16 (m, 1H), 6.86 – 6.80 (m, 4H), 5.89 (d, *J* = 3.1 Hz, 1H), 4.23 (s, 4H), 4.09 (dd, *J* = 7.0, 5.7 Hz, 1H), 4.02 (ddd, *J* = 7.0, 5.6, 3.8 Hz, 1H), 3.85 (dd, *J* = 5.8, 3.1 Hz, 1H), 3.77 (s, 6H), 3.51 (s, 3H), 3.47 – 3.41 (m, 2H), 3.38 – 3.32 (m, 2H), 2.74 (t, *J* = 7.2 Hz, 2H), 1.55 (t, *J* = 7.3 Hz, 2H), 1.49 (t, *J* = 7.1 Hz, 2H), 1.35 – 1.24 (m, 16H) ppm. ^{13}C NMR (151 MHz, $CDCl_3$) δ 164.0, 161.5, 158.6, 150.4, 145.9, 144.9, 136.0, 135.9, 130.3, 130.2, 128.3, 128.0, 126.9, 113.3, 113.3, 107.2, 89.1, 86.7, 83.6, 83.0, 70.0, 63.6, 58.9, 55.3, 41.5, 39.3, 32.5, 29.4, 29.3, 29.2, 29.2, 29.1, 29.1, 29.0, 26.8, 26.7 ppm.

1-((2R,3R,4R,5R)-5-((bis(4-methoxyphenyl)(phenyl)methoxy)methyl)-4-hydroxy-3-methoxytetrahydrofuran-2-yl)-2,4-dioxo-*N*-(12-palmitamidododecyl)-1,2,3,4-tetrahydropyrimidine-5-carboxamide **4**

To a clear solution of **3** (850 mg, 1.08 mmol) in anhydrous DCM (15ml) were added 2,5-dioxopyrrolidin-1-yl palmitate (458.18 mg, 1.30 mmol) and DIPEA (279.20 mg, 2.16 mmol, 376.27 µl) and the reaction mixture was allowed to stir at room temperature (rt) for 12 h. TLC showed complete consumption of the starting material. The volatile matters of the reaction mixture was concentrated under high vacuum pump to get the crude product which was purified by silica gel column chromatography eluting with 20%–50% EtOAc-hexane to afford **4** (1.03 g, 93% yield) as white foam. ^{1}H NMR (600 MHz, $CDCl_3$) δ 9.90 (d, *J* = 3.3 Hz, 1H), 8.41 – 8.31 (m, 2H), 7.25 (d, *J* = 7.8 Hz, 2H), 7.16 (dd, *J* = 8.5, 5.3 Hz, 3H), 7.07 (dd, *J* = 10.5, 5.6 Hz, 3H), 6.98 (dd, *J* = 8.1, 5.6 Hz, 1H), 6.68 – 6.59 (m, 4H), 5.70 (d, *J* = 3.1 Hz, 1H), 5.41 (t, *J* = 5.7 Hz, 1H), 3.93 (q, *J* = 6.8 Hz, 1H), 3.85 (dt, *J* = 10.0, 4.7 Hz, 1H), 3.68 (dd, *J* = 5.8, 3.1 Hz, 1H), 3.58 (d, *J* = 7.0 Hz, 6H), 3.37 – 3.30 (m, 3H), 3.26 (tt, *J* = 10.8, 6.5 Hz, 2H), 3.16 (dq, *J* = 12.7, 6.8 Hz, 2H), 3.03 (q, *J* = 6.8 Hz, 2H), 2.67 (dd, *J* = 7.7, 3.1 Hz, 1H), 1.95 (t, *J* = 7.7 Hz, 2H), 1.47 – 1.25 (m, 7H), 1.07 (d, *J* = 14.0 Hz, 42H), 0.68 (t, *J* = 6.9 Hz, 3H) ppm. ^{13}C NMR (151 MHz, $CDCl_3$) δ 173.3, 162.9, 161.2, 158.5, 149.5, 146.2, 144.8, 139.6, 135.9, 135.9, 130.2, 130.1, 129.2, 128.2, 127.9, 127.9, 127.8, 126.8, 113.3, 113.2, 113.2, 107.0, 89.2, 86.7, 83.6, 82.9, 69.8, 63.5, 58.9, 55.2, 39.6, 37.0, 32.0, 29.8, 29.7, 29.7, 29.6, 29.6, 29.5, 29.5, 29.4, 29.4, 29.3, 29.3, 27.1, 27.0, 25.9, 22.8, 14.2 ppm.

(2R,3R,4R,5R)-2-((bis(4-methoxyphenyl)(phenyl)methoxy)methyl)-5-(2,4-dioxo-5-((12-palmitamidododecyl)carbamoyl)-3,4-dihydropyrimidin-1(2H)-yl)-4-methoxytetrahydrofuran-3-yl (2-cyanoethyl) diisopropylphosphoramidite **5**

To a clear solution of **4** (900 mg, 877.74 µmol) in anhydrous DCM (10 ml) were added DIPEA (567.20 mg, 4.39 mmol, 764.42 µl) and NMI (144.13 mg, 1.76 mmol, 139.80 µl). The reaction mixture was allowed to stir for 5 min and then 2-cyanoethyl-*N*,*N*-diisopropylchlorophosphoramidite (415.49 mg, 1.76 mmol) was added and the reaction mixture was left at rt for additional 0.33 h. TLC showed complete consumption of the starting material. The reaction mixture was quenched with saturated aq $NaHCO_3$ and diluted with DCM. The organic layer was dried over Na_2SO_4 and filtered. Solvent was removed in rotary evaporator to get the crude product which was purified by silica gel column chromatography eluting with 20%–40% EtOAc-hexane to afford **5** (973 mg, 90% yield) as white foam. ^{1}H NMR (600 MHz, $CDCl_3$) δ 9.61 (s, 1H), 8.58 – 8.48 (m, 2H), 7.49 – 7.41 (m, 2H), 7.40 – 7.32 (m, 4H), 7.30 – 7.24 (m, 2H), 7.21 – 7.15 (m, 1H), 6.86 – 6.80 (m, 4H), 5.97 – 5.89 (m, 1H), 5.62 – 5.46 (m, 1H), 4.31 – 4.16 (m, 2H), 4.02 – 3.92 (m, 1H), 3.86 (ddd, *J* = 7.5, 6.0, 2.9 Hz, 2H), 3.79 – 3.76 (m, 6H), 3.55 (tdd, *J* = 16.9, 7.9, 5.3 Hz, 2H), 3.44 (d, *J* = 9.2 Hz, 3H), 3.39 – 3.31 (m, 3H), 3.22 (q, *J* = 6.7 Hz, 2H), 2.61 (q, *J* = 6.4 Hz, 1H), 2.34 (td, *J* = 6.4, 4.6 Hz, 1H), 2.14 (t, *J* = 7.6 Hz, 2H), 1.65 – 1.52 (m, 4H), 1.47 (t, *J* = 7.1 Hz, 2H), 1.37 – 1.19 (m, 43H), 1.15 (t, *J* = 6.3 Hz, 8H), 1.01 (d, *J* = 6.7 Hz, 4H), 0.87 (t, *J* = 7.0 Hz, 3H) ppm. ^{13}C NMR (151 MHz, $CDCl_3$) δ 173.3, 162.8, 161.2, 158.6, 158.5, 149.6, 146.3, 144.8, 144.7, 135.9, 135.7, 135.7, 130.3, 130.2, 130.2, 128.3, 128.2, 127.9, 126.8, 117.9, 117.6, 113.3, 113.3, 113.3, 113.2, 107.1, 107.0, 88.9, 88.8, 86.7, 86.7, 83.5, 83.4, 83.3, 82.3, 81.6, 71.1, 71.0, 70.6, 70.5, 63.3, 62.9, 58.8, 58.8, 58.8, 58.7, 58.4, 58.3, 58.0, 57.9, 55.2, 43.5, 43.4, 43.3, 43.2, 39.6, 39.5, 37.0, 32.0, 29.8, 29.8, 29.7, 29.7, 29.6, 29.6, 29.6, 29.5, 29.4, 29.4, 29.3, 27.1, 27.0, 25.9,

24.7, 24.6, 24.6, 22.8, 20.4, 20.4, 20.2, 20.2, 14.2 ppm. ^{31}P NMR (243 MHz, $CDCl_3$) δ 150.89, 150.20 ppm.

Oligonucleotide synthesis and purification

Oligonucleotides were synthesized on K & A Labs H-8 automated oligonucleotide synthesizer at 10 μmol scale using suitable supports. A solution of 0.25 M 5-(*S*-ethylthio)-1*H*-tetrazole in ACN was used as the activator. The solutions of commercially available phosphoramidites and synthesized phosphoramidities were used at 0.15 M in anhydrous ACN. The oxidizing reagent was 0.02 M I_2 in tetrahydrofuran(THF)/pyridine/H_2O. *N*,*N*-Dimethyl-*N*′-(3-thioxo-3H-1,2,4-dithiazol-5-yl)methanimidamide in 0.1 M in pyridine was used as the sulfurizing reagent. The detritylation reagent was 3% dichloroacetic acid in DCM. Detritylation of modified building blocks was performed manually using 3% TCA-DCM. Waiting times for coupling, capping, oxidation, and sulfurization step were 450, 25, 80, and 300 s, respectively. Lipid modified building blocks were coupled manually with two syringes and coupling time was 15 min. After completion of the automated synthesis, the oligonucleotide was manually released from support and deprotected using ammonium hydroxide/40% aqueous methylamine 1:1 v/v at rt for 3 h.

After filtration through a 0.45-μm nylon filter, oligonucleotides were quantified. For ion exchange, a preparative high-performance liquid chromatography (HPLC) column custom packed with TSKgel SuperQ-5PW (Sigma) was used. Appropriate gradients of mobile phase (buffer A: 20 mM sodium phosphate, 15% ACN, pH 8.5; buffer B: 1 M NaBr, 20 mM sodium phosphate, 15% ACN, pH 8.5) were employed. Oligonucleotides were desalted using size-exclusion chromatography using three Hi-Prep columns connected in series and water as an eluent. Oligonucleotides containing lipids were purified in reverse-phase (RP)-HPLC using appropriate gradient of buffer A (3% ACN in 50 mM aq triethylammonium acetate) and buffer B (80% ACN in 50 mM aq triethylammonium acetate) at ambient temperature (Supplementary Fig. S4). Pure fractions were concentrated in rotary evaporator at 36°C and desalted by size-exclusion chromatography using three Hi-Prep columns connected in series and water as an eluent. For sodium exchange, lyophilized powders were dissolved in 0.1 M sodium acetate and desalted again following the same desalting process. Oligonucleotides were then quantified by measuring the absorbance at 260 nm.

Extinction coefficients were calculated using the following extinction coefficients for each residue: A, 13.86; T/U, 7.92; C, 6.57; and g, 10.53 $M^{-1}\,cm^{-1}$. The identities of modified oligonucleotides were verified by mass spectrometry (Supplementary Table S1). Purities were evaluated by analytical RP-HPLC. For RP-HPLC, a C-18 column was used with a gradient of 2%–45% buffer B [buffer A: 95 mM hexafluoroisopropanol and 16.3 mM triethylamine (TEA), 0.05 mM ethylenediaminetetraacetic acid (EDTA); buffer B: MeOH] over 39 min. All the ion exchange (IEX)-HPLC were performed in DNAPac PA200 BioLC (4 × 250 mm) analytical column. Buffer A is 15% ACN and 20 mM sodium phosphate (pH 11), and buffer B is 15% ACN, 20 mM sodium phosphate, and 1 M NaBr (pH 11). A gradient of 31%–60% B over 12 min is used at 30°C. See Supplementary Table S1 for sequences of C5-lipid-modified oligonucleotides used for this study.

Measuring thermal stability for C5 modifications by UV-T_m

siRNA duplexes were annealed by heating at 94°C for 2 min followed by slow cooling. For T_m measurement, all the duplexes were used at 1 μM concentration in 0.1× phosphate-buffered saline (PBS). To minimize the possibility of any secondary structures cooling curve was recorded first by cooling the duplexes from 95°C to 25°C at a cooling rate of 1°C/min. For heating curve, the duplexes were heated from 25°C to 95°C at a heating rate of 1°C/min. For both cooling and heating curves, data were recorded in 1 min interval. The final T_m is the average of three heating curves and three cooling curves which has been provided in table.

HPLC-based hydrophobicity assay for C5 lipids containing duplexes and single strands

Retention time from non-denaturing ion-pairing reverse-phase high-performance liquid chromatography was used as a measure of duplex hydrophobicity. Duplexes were injected into C8 column (Agilent Poroshell 120 EC-C8: 2.1 × 100 mm, 2.7 μm, 120 Å) and eluted with suitable gradient using mobile phase A (100 mM TEAA) and B (100 mM triethylammonium acetate (TEAA) in 85% MeOH). For single strands hydrophobicity, C5-modification containing sense strands and controls were injected into C8 column (Waters XBridge® BEH C8 2.5 μM 2.1 mm × 50 mm) and eluted with suitable gradient using mobile phase A (95 mM hexafluoroisopropanol, 16.3 mM triethylamine, 50 μM EDTA) and B (MeOH).

Intraocular injections in mice

All animal experiments were approved by the Institutional Animal Care and Use Committee of University of Texas Southwestern Medical Center. The C57BL6J mice were purchased from the University of Texas Southwestern Mouse Breeding Core and equal number of age-matched litter-mate male and female mice were used when possible. Mice were given unlimited access to water and food and were on a 12-h light/12-h dark cycle.

Mice were anesthetized using intraperitoneal injections of ketamine/xylazine (120 mg/kg, 16 mg/kg, respectively) followed by dilation of pupils with one drop of phenylephrine 1% (Alcon) and 1 drop of tropicamide 2.5% (Alcon) 2 min afterwards. Upon full dilation, lubricant ointment eye gel (Henry Schein) was applied to the ocular surface to prevent desiccation of the corneas. The IVT injections were performed as previously described and guided using a Zeiss microscope [25].

The anti-*TTR* siRNAs were pre-formulated with 1× PBS to reach the desired concentration. A 30-gauge beveled needle was introduced either 1 mm posterior to the supero-lateral limbus at a 45-degree angle toward the vitreous cavity for IVT injection. The needle was inserted 1.5 mm deep into the eye and then carefully removed. The egressed chamber fluid was removed using a cotton tip applicator. A Hamilton microsyringe fitted to a 33-gauge beveled needle was placed in the previously fashioned needle tract and the solution was slowly injected in the eye. The needle was held in place for an additional minute after complete injection to allow cavity fluid equilibration with the injected solution. Post-injection AK-polysporin-bacitracin antibiotic ointment (Perrigo) was applied to the needle wound followed by a drop of the lubricant

gel. The mice were kept on a heating pad while recovering from the anesthesia.

Subcutaneous (SubQ) injections were administered into the loose skin over the mouse neck.

Ocular tissue harvest

Given the small amount of tissue available after dissection of the mouse eye, analysis of *TTR* mRNA levels by quantitative polymerase chain reaction (qPCR) is challenging and requires strict adherence to protocols. Following euthanization of the mouse, whole globes were enucleated at the optic nerve, rinsed with balanced salt solution (BSS), and then submerged in a small droplet of BSS in a 100 mm × 15 mm plastic petri dish. The globes were then punctured at the corneal limbus with a 30-gauge needle and circumferentially bisected along the limbus to separate the anterior and posterior segments. The neurosensory retinal tissue from the posterior chamber was carefully separated from the underlying RPE, choroid, and scleral tissue. These tissue layers were rinsed with BSS before storage. Whole corneal tissue from the anterior chamber was preserved after removal of lens and pigmented iris tissue. Lens capsule was peeled free and rinsed with BSS before storage.

Proceeding whole mouse corneal acquisition, the endothelial surface of the corneal tissue was incubated in trypan blue stain (Stephens Instruments) for two min before rinsed and re-submerged in BSS, allowing for enhanced visualization of the corneal endothelium apparent by the appearance of a thin translucent blue layer within the concave surface of the cupped cornea. Next, a 30-gauge needle was used to score the perimeter of the corneal endothelium. Then, forceps were used to grasp the stained endothelium edge followed by gentle separation of the thin blue endothelial layer from the underlying corneal stroma and epithelium. These tissue layers were then rinsed with BSS before storage.

All collected ocular tissues were inspected under high power microscopy for any signs of congenital, pathological, or procedure-related defects such as cataracts, opacities, fibrosis, or obvious signs of edema, which may indicate congenital malformations, procedure-related trauma or endophthalmitis, or abnormal wound healing. Any tissue with apparent defects was discarded and not used for quantitative analysis. Harvested corneal epithelium/stroma, corneal endothelium, lens capsule epithelium, neurosensory-retina, and RPE/choroid/scleral tissues together with liver tissue for siRNA-GalNAc were used to assess efficacy of TTR expression knockdown.

RNA extraction and qPCR analysis of TTR expression

Total RNA from corneal endothelium and lens capsule epithelium was extracted using RNeasy Micro Kit (Qiagen), RNA from corneal epithelium/stroma, retina, and RPE/choroid were extracted by RNeasy Mini kit (Qiagen). Tissues were lysed using a homogenizer for 30 s to 1 min with interval, other steps were followed according to the manufacturer's protocol. Complementary DNAs were made by reverse transcription with a high-capacity reverse transcription kit (Applied Biosystems) per the manufacturer's protocol using equal amount of RNAs from tissue samples. qPCR experiments were performed on a CFX96 Touch real-time PCR system (Bio-Rad) using iTaq SYBR Green Supermix (Bio-Rad). PCR reactions were done in triplicates at 55°C 2 min, 95°C 3 min, and 95°C 30 s, 60°C 30 s for 40 cycles in an optical 96-well plate. Data were normalized relative to levels of reference gene *RPL19* mRNA. Mouse *TTR* primers: F, 5′-CGTACTGGAAGACACTTGGCATT-3′; R, 5′-GAGTCGTTGGCTGTGAAAACC-3′. Mouse RPL19 primers: F 5′-GTATGCTCAGGCTACAGAAGAG-3′; R 5′-GAGTTGGCATTGGCGATTT-3′. The final data were analyzed using GraphPad Prism 8 software.

Results

Lipid conjugate design and synthesis

Duplex RNAs were synthesized with a mixture of 2′-F and 2′-Ome nucleotides to improve *in vivo* stability and activity (Fig. 1 and Supplementary Table S1). PS or an L8 hydroxyprolinol linker [26] were included at termini to improve resistance to degradation by nucleases. VP modification was used at 5′-end of antisense strand [27].

The length and attachment point of the lipid chain can affect binding to soluble proteins and membranes, affecting the biodistribution of nucleic acids. C16 lipid chains were attached via the C5 position of a pyrimidine nucleobase (TTRa–C5–C16) or the O2′ position of the ribose (TTRb–O2′–C16). TTRb–C5–C28 had a C28 lipid chain conjugated to the C5 position of the nucleobase.

TTRa–GalNAc has the same sequence as TTRa–C5–C16, but the GalNAc is attached at the 3′-end of sense strand with a hydroxyprolinol linker. TTRa–GalNAc is similar in design to the approved drug Vutrisiran [13]. TTRa and TTRb lack the conjugated lipid but have similar chemical modifications to TTRa–C5–C16 and TTRb–O2′–C16/TTRb–C5–C28, respectively. Control-1 and Control-2 have similar arrangements of chemical modifications as TTRb–O2′–C16/TTRb–C5–C28 but lack complementarity to TTR mRNA.

For compound TTRa–C5–C16, we first synthesized hexadecyl lipid chain containing 2′-*O*-methyluridine phosphoramidite (Fig. 2A and Supplementary Fig. S1) where the lipid chain was present at C5 position of the nucleobase. Activated trifluoro ester (C5-TFE ester) [24] was heated with 1-aminohexadecane to get compound **1** via amide bond formation. Compound **1** was then employed for phosphoramidite synthesis using standard protocol to produce lipophilic phosphoramidite **2** in good yield which was incorporated in sense strands of siRNA using standard oligonucleotides synthesis protocols.

With compound TTRb–C5–C28, we explored the role of longer lipid chain by synthesizing C28-lipid containing phosphoramidite (Fig. 2B). First, activated trifluoro ester (C5-TFE ester) was heated with 1,12-diaminododecane to obtain compound **3** via amide bond formation. Compound **3** was then reacted with commercially available *N*-hydroxysuccinimide ester of hexadecenoic acid for a second amide bond formation to have compound **4** which was finally employed for phosphoramidite synthesis using standard protocol to have lipophilic phosphoramidite **5** in good yield.

Effect of C5-lipid attachment in the context of duplex relative to single strands

Hydrophobicity is one of the critical determinants of biodistribution. To evaluate the hydrophobicity contribution from C5-lipids attached to single strands relative to duplexes we used

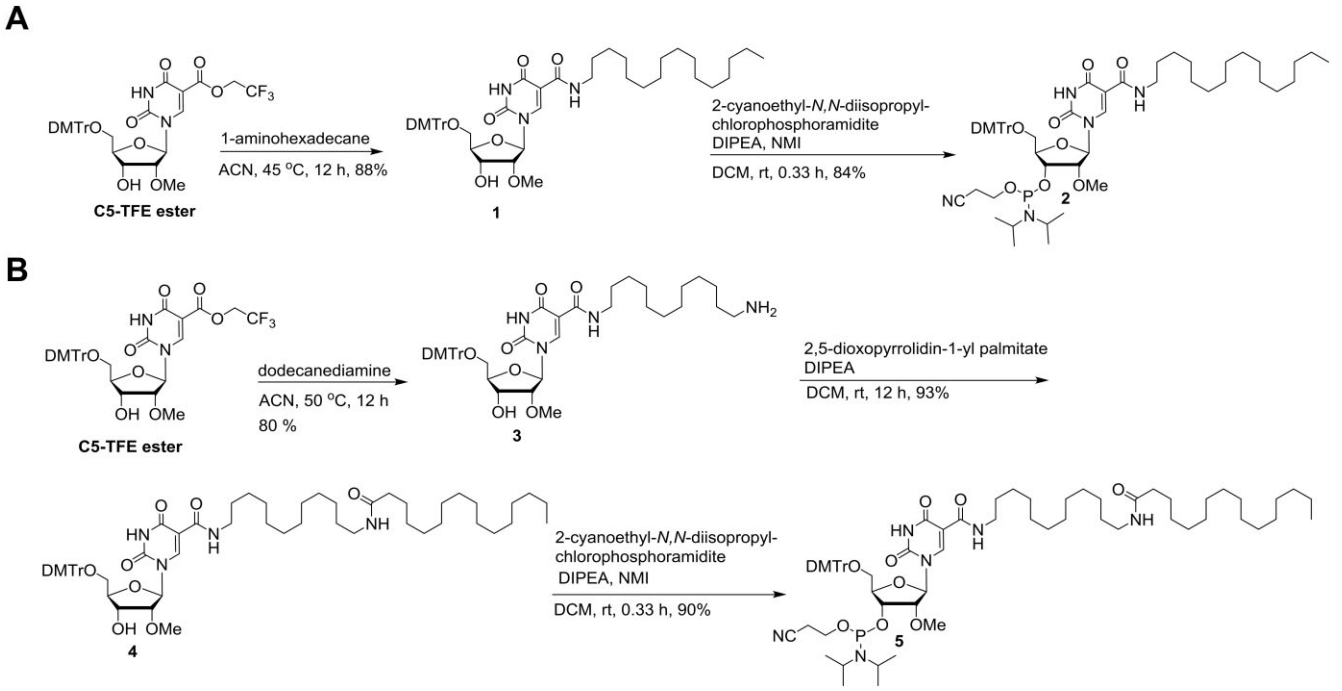

Figure 2. (**A**) Synthesis of C5 C16-lipid chain containing 2′-*O*-methyluridine phosphoramidite. (**B**) Synthesis of C5 C28-lipid chain containing 2′-*O*-methyluridine phosphoramidite.

RP-HPLC (Supplementary Fig. S2). As expected, both TTRb–C16 and TTRb–C28 were more hydrophobic than TTRb regardless of whether the modified strand was single-stranded or in a duplex. C28 conjugation had a bigger impact than attachment of C16, as would be expected from the longer C28 lipid chain.

The impact for C28 relative to C16, however, was much greater in the single stranded context. For single strands, C28-lipid at C5 position of uridine showed almost 5-min delay in elution (13.5 min) as compared with standard 2′-O-C16 lipid (8.5 min). In duplexes, by contrast, C28-lipidated duplex TTRb–C5–C28 showed only 1.3-min elution delay (11.3 min) with respect to 2′-O-C16 lipid (10.0 min) duplex TTRb–O2′–C16. One explanation for the muted impact of C28 on hydrophobicity of lipidated duplexes is that the lipid is less able to bind into the major groove when attached at C5 than when attached at O2′, making interactions with the reverse phase matrix more likely.

Thermal melting studies revealed that duplex RNA TTRb–C5–C28 is thermally destabilized by 8.0 degrees as compared with control (no lipid) duplex TTRb whereas TTRb–O2′–C16 is only 1.5 degrees destabilized relative to TTRb (Supplementary Fig. S3 and Supplementary Table S2). This is consistent with the lipid component of TTRb–C5–C28 having fewer stabilizing interactions with the RNA duplex.

In vitro evaluation of dsRNA conjugates

Attachment of lipid or GalNAc moieties to an siRNA might affect the intrinsic silencing potency of the duplex, independent of any positive effects on biodistribution. To test whether this was occurring, we transfected unmodified control duplexes TTRa and TTRb into mouse BNL CL2 liver cell line and compared their activities with modified duplexes TTRa–C5–C16, TTRb–O2′–C16, TTRb–C5–C28, and TTRa–GalNAc. Spontaneous uptake of lipid-modified siRNAs is not efficient in cultured cells and was facilitated using the cationic lipid RNAiMAX.

Attachment of C16 at C5 to create TTRa–C5–C16 had little effect on potency when evaluated relative to the unconjugated duplex TTRa in cultured cells (Fig. 3A). IC_{50} values were ∼1–3 nM regardless of whether the lipid was attached. Unmodified duplex TTRb was much less potent than TTRa, indicating that the chemical modification pattern used for the TTRb series of compounds reduces potency. This deficit, however, was rescued by attachment of lipid as both TTRb–O2′–C16 and TTRb–C5–C28 were like the potency of TTRa–C5–C16 (Fig. 3B). This surprising result may indicate that the chemical modification pattern used in the TTRb series reduces *in vitro* potency which is then rescued by attachment of lipid. Alternatively, the result could be due to improved binding of the siRNA–lipid by the transfection reagent. These data suggest that lipid-modified RNA duplexes have good potencies inside cells in culture and supported further testing in mice.

We also evaluated the GalNAc to 3′-terminus of the passenger strand because to evaluate whether conjugates that are like the approved drug Vutrisiran. We observed that the attachment of GalNAc to TTRa reduced potency in cell culture with an IC_{50} value of ∼12 nM (Fig. 3C). GalNAc conjugation, despite immense value for the success of *in vivo* drug development, may be at a slight disadvantage relative to lipid conjugates for fundamental intracellular silencing.

Gene silencing throughout the eye

Our goal was to analyze tissues from both the anterior and posterior segments of the mouse eye including the RPE (Fig. 4A). The eye is a complex organ composed of tissues with diverse functions that offer different drug targets and opportunities of oligonucleotide drug development. It is important, therefore, to analyze the different parts of the eye separately.

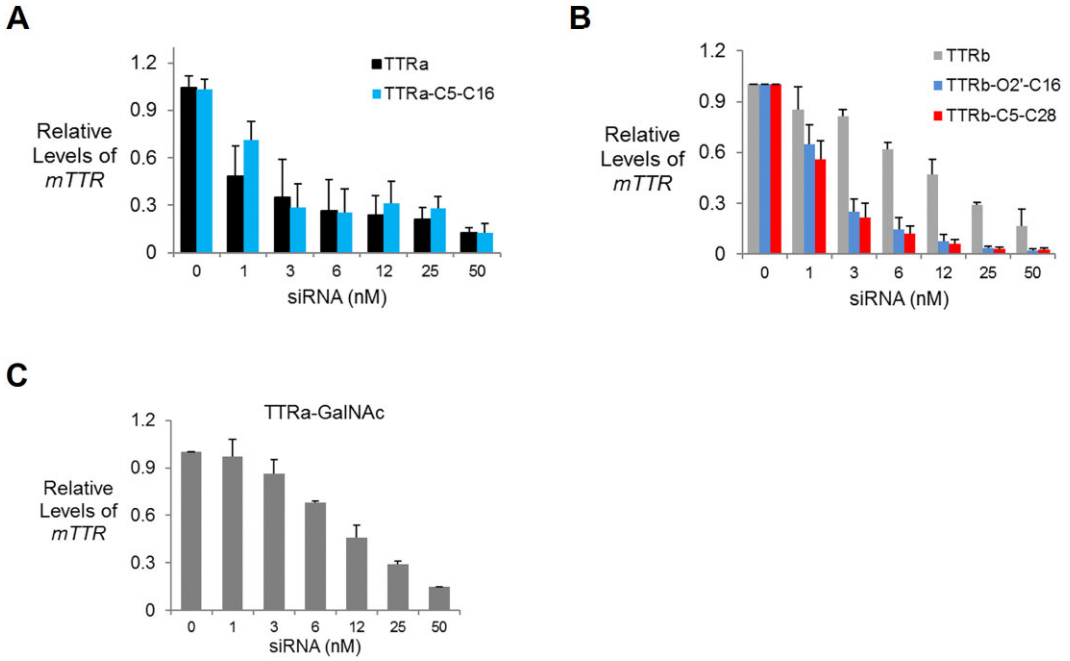

Figure 3. *TTR* gene expression after transfection of lipid-modified double-stranded RNAs (dsRNAs) into BNL CL2 murine cells using RNAiMAX as a transfection reagent. (**A**) TTRa and TTRa–C5–C16. (**B**) TTRb, TTRb–O2′–C16, and TTRb–C5–C28. (**C**) TTRa–GalNAc. Error bars are mean with SEM. $N = 4$ independent replicates.

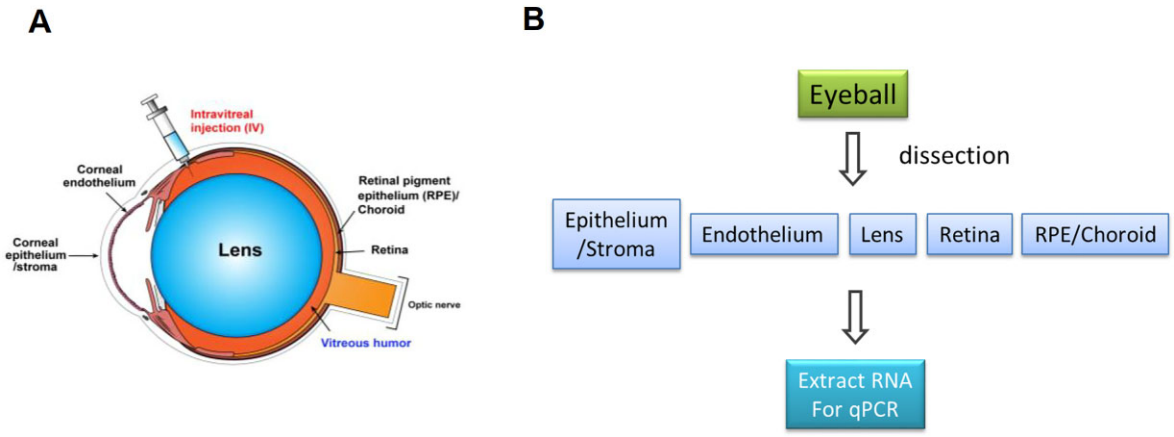

Figure 4. Strategy for ocular injections and analysis. (**A**) Schematic for the murine eye. (**B**) Scheme for dissection and tissue analysis. Tissue was harvested 7 days after IVT injection.

In the mouse eye, this approach is challenged by the small amounts of critical tissues and the associated need to microdissect samples.

While we examined TTR expression throughout eye, the RPE is the primary tissue involved with ocular ATTR. The RPE is a continuous monolayer of post-mitotic cells located between the neurosensory retina and the choroid, the vascular connective tissue layer that nourishes the outer retina. The lateral membranes of the RPE cells are joined by a continuous belt of tight junctions that form the outer blood–retina barrier [28]. The RPE is metabolically active in its maintenance role of photoreceptor layer by regulating the flow of nutrients and waste products to and from the retina and renewal of the spent outer segments of the photoreceptors. Ocular production of mutant TTR by the RPE is thought to result in ATTR eye disease findings [19, 20, 23].

siRNAs were formulated in PBS and administered by IVT injection to test their effects on *TTR* expression. We had previously observed that delivery of anti-MALAT1 ASOs by IVT was more effective than delivery by intracameral injection into the anterior chamber [29]. Tissue was harvested from the corneal epithelium/stroma, corneal endothelium, the lens, the neurosensory retina, and the RPE/choroid layers (Fig. 4B). We processed these tissues and evaluated expression using qPCR.

Prior to testing conjugates in mice, we evaluated the relative expression of *TTR* mRNA in different eye tissues (Fig. 5). *TTR* was expressed most highly in the RPE, consistent with the previous observation that cultured RPE cells synthesize and secrete the TTR protein [22, 30]. Expression of *TTR* mRNA was 40-fold higher in RPE/choroid than retina and 40- to 10 000-fold higher than in lens, corneal endothelium, or corneal epithelium/stroma.

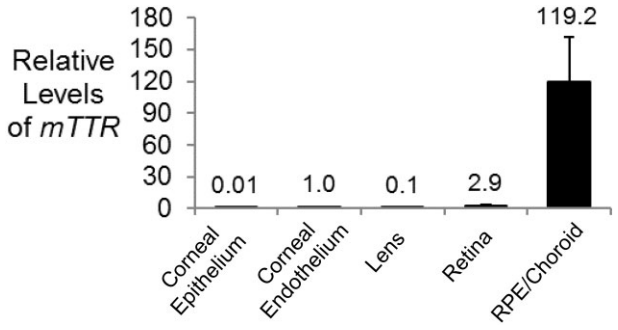

Figure 5. Relative expression of *TTR* mRNA in different murine ocular tissues measured by qPCR. Data were normalized relative to levels of murine *RPL19*. Error bars are mean with SEM. $N = 4$ independent replicates.

Testing of C5-linked C16 conjugate in mice administered by IVT injection

We began by analyzing the effect of siRNA conjugate TTRa–C5–C16 on *TTR* expression in mouse RPE/choroid, lens, corneal endothelium, corneal epithelium/stroma, and retina (Fig. 6). Two mice were injected with 50 μg compound per eye for each experimental group (Fig. 6A–E). For all tissues, >80% inhibition was achieved relative to eyes injected with PBS or Control-1 duplex RNA. This initial testing demonstrated that siRNA conjugates had the potential to inhibit gene expression in all parts of the mouse eye. We then examined inhibition as a function of concentration of conjugates TTRa and TTRa–C5–C16 in the RPE. Inhibition of *TTR* expression was not efficient at when <9 μg was injected, suggesting a need for more potent designs for ocular use of lipid-conjugated siRNAs (Fig. 6F and G).

Testing of C5-linked C28 and 2′-OC16 conjugate in mice

We reasoned that altering the point of lipid attachment or the length of the lipid chain as well as modifying the siRNA design might enhance potency. To test this hypothesis, we evaluated siRNA duplexes TTRb, with 2′-O linked conjugate TTRb–O2′–C16, and C5-linked conjugate TTRb–C5–C28 (Fig. 7). As further described below, modeling suggests that both TTRb–O2′–C16 and TTRb–C5–C28 have improved potential to have necessary protein interactions that might affect biodistribution and delivery to cells. These duplexes also have a different pattern of modifications than TTRa–C5–C16 that has been observed to offer improved potencies against other targets. This new generation of compounds was chosen for detailed dose response analysis over a range of concentrations.

We observed that TTRb, the siRNA that lacked lipid modification, inhibited *TTR* expression but only at the highest dose (50 μg) in RPE/choroid (Fig. 7A). By contrast, conjugates TTRb–O2′–C16 and TTRb–C5–C28 were more potent inhibitors, with >90% inhibition when 9 μg were injected and ~50% inhibition after injection of as little as 0.3–1 μg. Duplex RNA Control-2 had no significant effect on RPE/choroid expression, even when administered at the highest dose. TTRb–C5–C28 achieves potent gene silencing even though thermal melting studies reveal that it has a significantly lower T_m than TTRb or TTRb–O2′–C16 (Supplementary Table S2 and Supplementary Fig. S2).

While the RPE is an important source of production of the mutant TTR protein responsible for ATTR ocular pathology, we also examined the effect of siRNAs on *TTR* expression in other parts of the eye, including lens, corneal endothelium, corneal epithelium/stroma, and retina (Fig. 7B–E). Measuring the effects of dsRNA-modulated *TTR* gene expression in these tissues of the eye is more challenging because of the low levels of *TTR* RNA relative to RPE/choroid. While there was greater uncertainty in the data, we observed clear trends showing the potential of lipid-modified siRNAs to broadly inhibit gene expression in tissues of both the anterior and posterior segment of the eye.

Inhibition of TTR expression by GalNAc conjugates

A GalNAc conjugate, TTRa–GalNAc (Fig. 1), is like the conjugate siRNA already approved to treat ATTR. Our goal was to test whether it could also inhibit TTR expression in the eye. TTRa–GalNAc was administered either systemically by SubQ injection or directly into the eye by IVT injection.

When administered SubQ, TTRa–GalNAc inhibited *TTR* gene expression in the liver at ~90% (Fig. 8A), consistent with the known hepatic efficacy of GalNAc conjugates. *TTR* expression after SubQ administration was not inhibited in the RPE, consistent with the bloodstream eye barrier [21, 28] (Fig. 8B). When TTRa–GalNAc was injected into the eye by IVT at 50 μg, inhibition of *TTR* mRNA expression was observed (Fig. 8B). IVT injection of TTRa–GalNAc had no effect on *TTR* expression in the liver (Fig. 8A), consistent with the presence of an ocular/blood barrier and the small amount of compound injected into the eye.

Modeling of the binding of human serum albumin to siRNAs with different lipid modifications at the C5 position

TTRa–C5–C16 and TTRb–C5–C28 share a common attachment for the lipid chain to the C5 position of uridine 6 of the sense strand (Fig. 1). While TTRb–C5–C28 was a potent *in vivo* silencing agent for *TTR* gene expression (Fig. 7), TTRa–C5–C16 was less potent (Fig. 6G). These data suggest that the lipid length affects the efficacy of lipidated siRNAs. To gain insight into how the length of the lipid or point of attachment might contribute to the different activities of siRNAs tested in this report, TTRa–C5–C16, TTRb–O2′–C16, and TTRb–C5–C28 (Fig. 1), we turned to human serum albumin (HSA) as a model system for protein–lipid interactions.

HSA interacts with synthetic oligonucleotides and plays an important role governing the systemic biodistribution of therapeutic nucleic acids [26, 31, 32], HSA is also the dominant soluble protein in vitreous fluid [33], suggesting that it has the potential to form interactions that impact the biodistribution and activity of therapeutic oligonucleotides in the eye. Albumin as a carrier biomaterial for ocular delivery has been recently reviewed emphasizing the improved pharmacokinetics, sustained release, and improved pharmacology [34].

To evaluate the accessibility of lipid chains for interactions with HSA, we examined the crystal structure of HSA in complex with myristic acid (C14) (Supplementary Fig. S5) determined at a resolution of 1.9 Å that shows eight bound fatty acid molecules (PDB ID 8RCP) [35]. We chose one of the myristic acid molecules with the carboxylate located near the protein surface. Using the UCSF Chimera graphic software package [36], we converted the carboxylate carbon to methy-

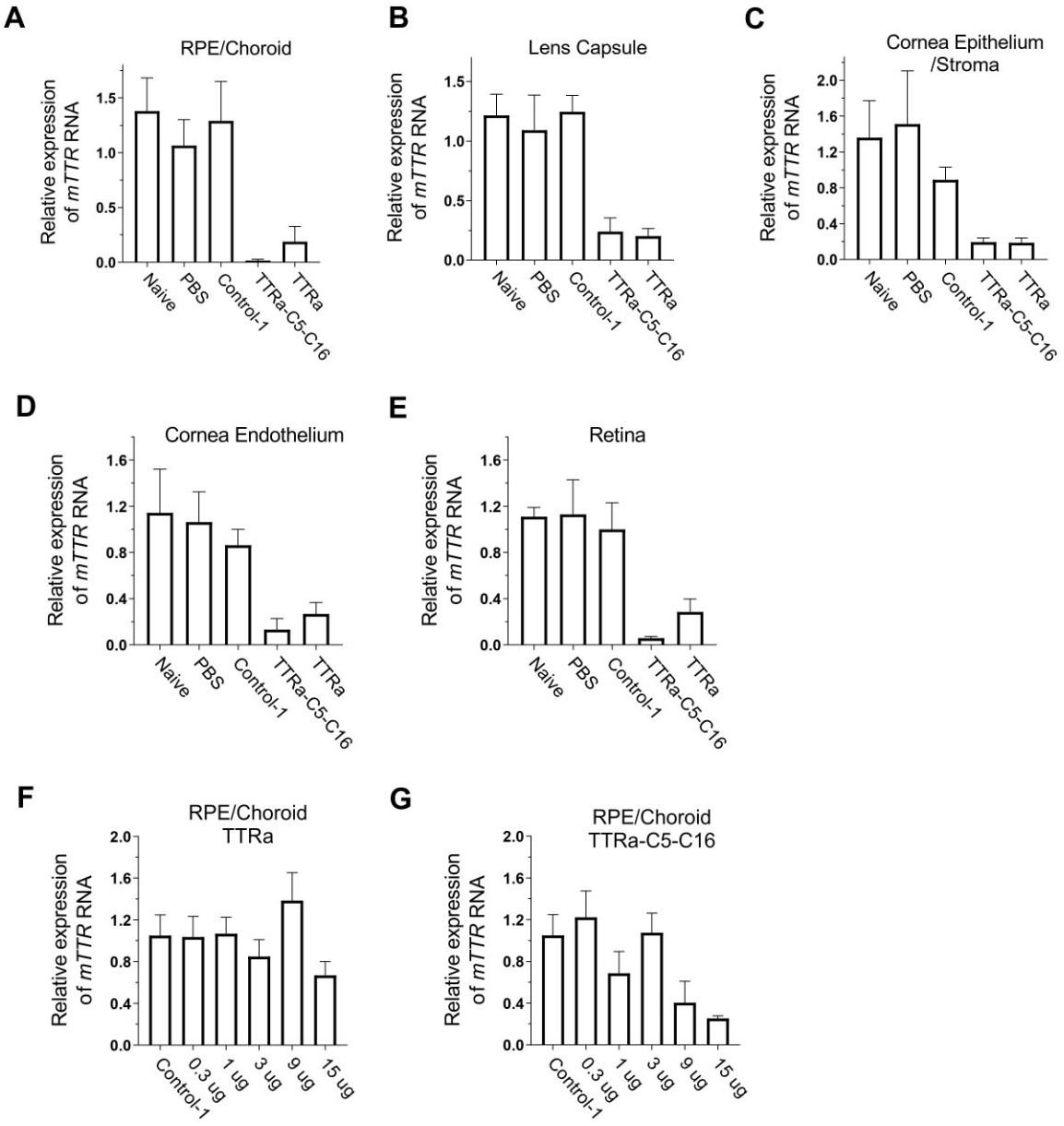

Figure 6. Inhibition of *TTR* gene expression by dsRNAs administered (IVT) at 50 μg per eye. (**A**) RPE/choroid. (**B**) Lens capsule. (**C**) Corneal epithelium/stroma (**D**) Corneal endothelium. (**E**) Retina. (**F**, **G**) Dose response for TTRa and TTRa–C5–C16. Tissue was harvested 7 days after injection. Data were normalized relative to levels of murine *RPL19*. Error bars are mean with SEM. $N = 4$ independent replicates.

lene and extended the chain to C16. We first modeled C16 attached to the 2′-O. The TTR siRNA model was generated in 3DNA [37] and then combined with the modified serum albumin–myristic acid complex to build the TTRb–O2′–C16 conjugate bound to albumin.

The lipid chain, now extended from C14 to C16, slightly protrudes from the albumin surface (Fig. 9A). Using UCSF Chimera, the siRNA duplex together with torsion angles around the C13–C14 and C14–C15 bonds of the lipid were manipulated such that O2′ of sense strand U6 and the terminal methylene of the C16 chain were positioned for bond formation between the lipid and O2′ located in the shallow grove. The final model of TTRb–O2′–C16 does not exhibit unfavorable contacts between albumin and siRNA, all torsion angles along the C16 chain are in the *ap* or *ac* ranges, and the binding mode of the myristic acid portion of the C16 chain is that observed in the crystal structure of the complex (Fig. 9A). This modeling suggests that the attachment of C16 to O2′ permits substantial interactions between lipid and HSA.

We next evaluated C16 and C28 carbon chains attached at the C5 position. While we do not show the C16 chain separately, it can be visualized as a subset of the C28 chain. We observed that the C16 chain is too short to link the lipid bound to albumin to the C5 position of U6 that is located at the floor of the narrow and deep major groove (Fig. 9B). This helps rationalize the lack of activity seen with TTRa–C5–C16—it is too short to escape the deep and narrow groove of the A-form siRNA duplex and form interactions with proteins like HSA.

The model we built of the TTRb–C5–C28 siRNA duplex bound to albumin is free of unfavorable contacts between RNA and protein. In contrast to the C16 lipid, TTRb–C5–C28 has a lipid chain that is long enough to form an

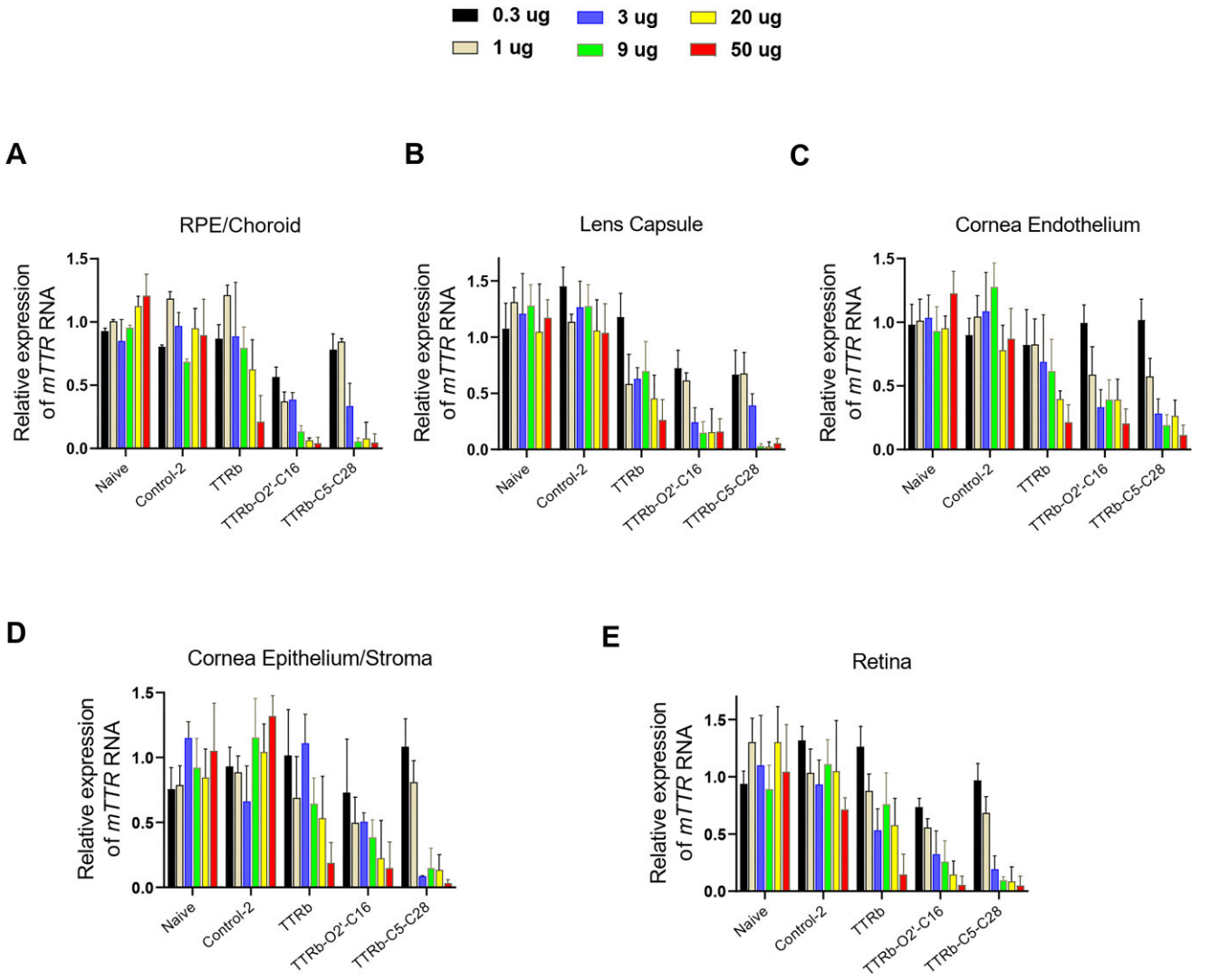

Figure 7. Inhibition of *TTR* gene expression in the RPE by dsRNAs TTRb–O2′–C16 and TTRb–C5–C28 at varying concentrations. Tissue was harvested 7 days after IVT injection. Data were normalized relative to levels of murine *RPL19*. Error bars are mean with SEM. $N = 4$ independent replicates.

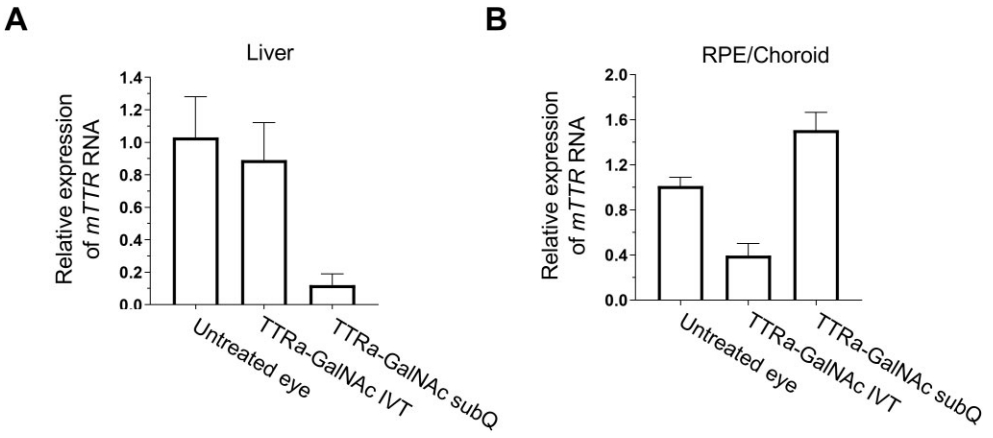

Figure 8. Inhibition of *TTR* gene expression in the RPE by dsRNA TTRa–GalNAc in mouse RPE and liver. (**A**) Expression levels of *TTR* in mouse liver. (**B**) Expression levels in RPE/choroid. Tissue was harvested 7 days after injection of 3 μg (IVT) or 50 μg (SubQ). Data were normalized relative to levels of murine *RPL19*. Error bars are mean with SEM. $N = 4$ independent replicates.

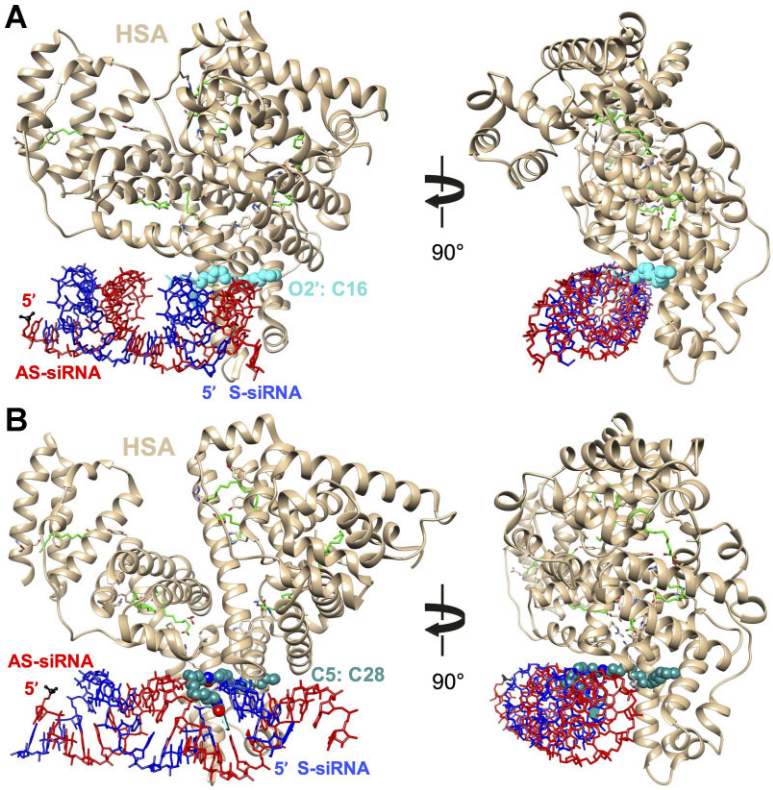

Figure 9. Computational models of the (**A**) TTRb–O2′–C16 and (**B**) TTRb–C5–C28 siRNA duplexes bound to HSA based on the crystal structure of the albumin–myristic acid complex (PDB ID 8RCP). TTRa–C5–C16 can be imagined as a subset of the TTRb–C5–C28 model shown in panel (B). The views are across the major and minor grooves of the RNA duplex (left) and then rotated around the vertical by ca. 90 degrees and more along the helical axis (right). Albumin is depicted in cartoon mode and colored in tan and carbon atoms of fatty acid molecules are green. Bonds of siRNA antisense and sense strands are colored in red and blue, respectively, the 5′-terminal phosphate group of the former is highlighted in black and ball-and-stick mode (bottom left corner of figure panels on the left).

interface with HSA (Fig. 9B). This model supports the hypothesis that the longer lipid chain allows greater binding to protein and may enhance potency *in vivo*. We note that this improved potency is achieved despite the intrinsic silencing of the nonlipid-modified parent duplex of TTRb–C5–C28, TTRb being poorer than the intrinsic potency of TTRa–C5–C16 (Fig. 3).

Analysis of the binding of Argonaute 2 (Ago2) to siRNAs modified with C16 chains at O2′ or C5 positions

Next, we turned our attention to the interaction between siRNA–lipid conjugates and Argonaute2 (Ago2) endonuclease. Ago2 is the "slicer" enzyme that both promotes binding of siRNA guide strands to mRNA targets. Ago 2 is a critical member of the RNA-induced silencing complex and cleaves mRNA targets to amplify potency. Because of its central role in RNAi, interactions between Ago2 and the lipid chains may affect the potency of lipidated duplex RNA conjugates.

We modeled how attachment of C16 lipid at either the O2′ and C5 positions would affect association with Ago2. To build models of an siRNA duplex with O2′–C16 or C5–C16 conjugates bound to Ago2, we used the crystal structure of the enzyme in complex with miR-122 bound to a target RNA determined at a resolution of 3.4 Å (PDB ID 6MDZ) [38]. We used UCSF Chimera to attach C16 chains to the O2′ and C5 positions and maintain C16 torsion angles in the ap and ac ranges. The C16 chain attached to O2′ in the shallow minor groove is almost completely exposed on the surface of the RNA duplex (Fig. 10, cyan chain), allowing it to efficiently interact with lipid binding proteins and membranes.

Like the C16 portion in our model of the TTRb–C5–C28 lipid siRNA conjugate bound to HSA (Fig. 9B), the C16 chain attached to C5 barely emerges from the deep major groove (Fig. 10, pink and magenta chains adopt alternative conformations). Only four methylene moieties lie outside the groove, thereby illustrating that the C28 conjugate is needed to escape the major groove and present a sufficiently long lipid chain for stable interaction with molecules other than Ago2. The models of C16 chains (Fig. 10) do not result in any short contacts to Ago2. If contacts beyond Ago2 contribute to the potency of lipidated C5 conjugates, C28 may have advantages versus C16.

Discussion

Expanding options for siRNA conjugates

Devising strategies for extra-hepatic delivery is the defining challenge for the development of nucleic acid therapeutics. The introduction of new conjugate types, lipids in this case, variations in the length of the chain, and the sites for attaching them help expand the repertoire of chemical tools for delivery to organs beyond liver. Potential beneficial effects include improvements in pharmacokinetics and pharmacodynamics, as well as better control of off-target effects. The exploration of new chemistries paves the road to gains in potency and safety, sometimes in ways that are not now evident.

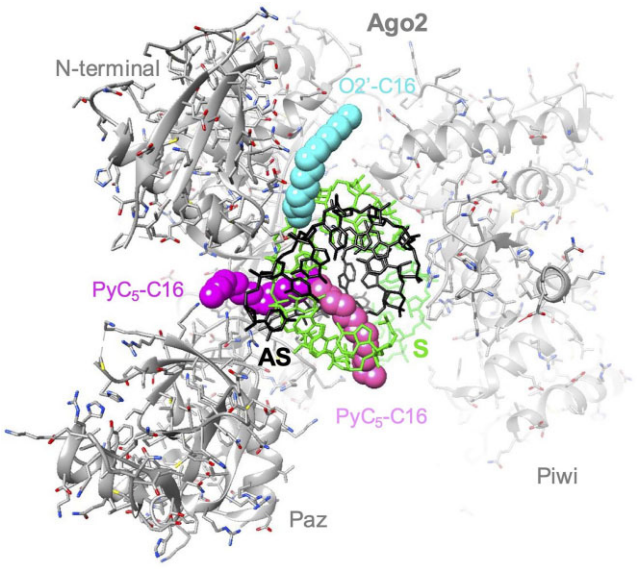

Figure 10. Computational models of human Ago2 in complex with an siRNA antisense (AS, black bonds)-sense (S, green bonds) strand duplex with C16 lipid conjugates attached to the O2′ or C5 positions of sense strand residue U6 based on the crystal structure of Ago2 bound to miR-122 opposite a target RNA (PDB ID 6MDZ). Ago2 is depicted in cartoon mode and colored in gray with individual domains labeled (the MID domain is invisible in the background). Carbon atoms of the C16 chain attached to O2′ are colored in cyan. The C16 chain attached to C5 was modeled in two alternative conformations, one emerging from the center of the major groove (carbon atoms colored in pink) and the other wrapping around the backbone of the antisense siRNA to escape the groove (carbon atoms colored in magenta).

Ocular efficacy of lipid-conjugated siRNAs

Our primary goal was to test whether GalNAc and lipid-modified siRNAs could inhibit *TTR* gene expression in varied tissues within the mouse eye. A secondary goal was to explore how changing the length (C16 or C28) of the lipid chain or its point of attachment. (C5 or 2-O′) to the nucleotide would affect gene silencing. Our data from both C5 and 2′O-linked conjugates demonstrate inhibition in a broader range of ocular tissues, encouraging future exploration of gene silencing by lipid-modified siRNAs in tissues beyond the RPE. C16 and C28 conjugates tested after IVT injection inhibited gene expression in both the anterior and posterior segments of the eye, including the RPE/choroid, retina, lens, corneal endothelium, and corneal epithelium/stroma. Inhibition in all tissues was achieved even though *TTR* expression varies by 10 000-fold in these tissues.

Designing base-modified (C5-uridine) lipid conjugates

Previous work had examined attachment of a C16 lipid chain at the 2′-O position of uridine [9]. The 2′-hydroxyl group allows for particularly facile attachment of substituents and linkers but could become problematic in a regiospecific fashion if the residue or ribose were engaged in protein–RNA interactions. The chemical stability of the major groove nucleobase site of attachment could be beneficial compared with the 2′-OH. Moreover, for oligomers like morpholino or PNA that typically lack a 2′-OH or similar functionality, C5 becomes more important.

We hypothesized that accessibility of the lipid chain for interactions with proteins would affect biodistribution and activity. To explore this concept, we initially synthesized C16 lipid conjugates at C5 position of uridine from activated trifluoro ester [24] (Figs 1 and 2). Initial *in vivo* study revealed that C16 lipid conjugate at the C5 position (TTRa–C5–C16) yielded only modest improvement in potency relative to the analogous nonlipidated control (TTRa) (Fig. 6). An RP-HPLC based hydrophobicity assay revealed that the C5–C16 conjugation contributes less hydrophobicity to the siRNA duplex than it does to the corresponding single strand, suggesting that the duplex blocks interactions with the C5-conjugated lipid chain.

After these observations we explored the activities of conjugates containing a longer lipid at C5, TTRb–C5–C28, or a lipid conjugated at the 2′-O position (TTRb–O2′–C16). Modeling studies suggested C16 lipid attached at the C5 position form interactions with the major groove of the siRNA. These interactions would obstruct interactions between the lipid chains and proteins like HSA or Ago2 (Figs 9 and 10) and might contribute to reduced potency. Modeling also suggested that a longer C5-linked lipid chain (TTRb–C5–C28) or a 2′-O linked lipid (TTRb–O2′–C16) would be more accessible. For C5 conjugates, the modeling suggests that the lipid should be at least 24 carbons.

Our experimental assays support these suggestions. TTRb–C5–C28 achieves a similar potency to the 2′-O linked conjugate TTRb–O2′–C16. While we acknowledge that more work will be necessary to substantiate our hypotheses connecting conjugated design, structure, and function, our data, however, showing robust silencing by TTRb–O2′–C16 and TTRb–C5–C28 (Fig. 7), suggests that strategic choice of lipid structure and placement can improve gene silencing.

Potential for interactions between lipid-modified siRNAs and albumin

Our hypothesis was that the position of lipid conjugation could affect the silencing potential of siRNAs *in vivo* in the eye. While our data support this hypothesis, subsequent studies will be necessary before a definitive conclusion can be made. The binding affinities of fatty acids for albumin were reported in detail many years ago [39]. In the case of palmitic acid, the association constant (K_1, as multiple fatty acid molecules are bound) is 2.55×10^8 M [40]. Further evidence for tight binding between fatty acids and albumin is provided by the crystal structure of myristic acid (eight individual molecules) bound to albumin (PDB ID 8RCP) [35]. We used that structure as the basis to build the model of the siRNA-conjugated C16 and C28 chains bound to the protein.

Interestingly, this team also reported crystal structures of albumin in complex with aristolochic acids I and II (AA-I and -II), carcinogenic compounds of Aristolochia plants. The K_d values for these small molecule binders were up to 690 nM and the crystal structures demonstrated that not all myristic acid molecules were displaced from albumin in the presence of AA-I or -II. This is fully consistent with the 2.1×10^7 M association constant for myristic acid binding to albumin as per the above paper by Ashbrook *et al.* [40].

Therefore, the tight association of fatty acids with albumin is well documented and it is not a stretch to assume that long lipid chains conjugated to siRNA will be captured by serum albumin in the cell, thereby aiding in siRNA biodis-

tribution and ultimately potency. That said, it is still of interest to eventually measure the binding affinity between C16- and C28-conjugated siRNAs and albumin. ASO-small molecule binding to albumin has been well documented [41]. Sleiman and colleagues have reported methods for measuring oligonucleotide–lipid conjugates to albumin [42]. Similar experiments with siRNA–lipid conjugates are evolving and should complement future structure activity relationship analyses [43].

Finally, it is important to note that we have tested a small number of compounds. Our study was limited by the resource-intensive nature of compound testing with detailed tissue analysis in the mouse eye, especially in an academic setting. Subsequent studies that test additional compounds would likely reveal significant mechanistic insights and the potential for even more potent silencing agents.

Conjugate site affects siRNA duplex stability

The difference in the thermal stability of the TTRb–C5–C28 and TTRb–O2′–C16 duplexes—almost 7°C in favor of the latter—is striking (Supplementary Fig. S3 and Supplementary Table S2). While we acknowledge that lipid:RNA interactions are not well understood, we speculate that both steric and electrostatic factors may contribute to the greater loss in stability caused by the longer lipid chain.

Compared with the association between lipid and a carrier protein like HSA, little is known about the association between a lipid and an RNA duplex. Currently, we lack insights regarding the relative contributions of enthalpy and entropy to the differential free energies of melting for the two duplexes, e.g. from a van't Hoff analysis. However, we can assume that the lipid chain attached to the 2′-O will not be hindered in its mobility to the same extent as the chain attached to C5 buried at the floor of the major groove. This discrepancy is expected to unfavorably affect the entropic change upon duplex formation for TTRb–C5–C28 relative to TTRb–O2′–C16. Further, considering the groove location of the lipid chain attached to C5, we can speculate that both steric and electrostatic factors contribute to the greater loss in stability caused by the longer C28 chain.

It is challenging to accommodate the hydrophobic and flexible chain inside the deep and narrow RNA major groove, a site of limited space and strong negative electrostatic potential. The portion of this chain (amounting to at least half its length) that is buried inside the groove will interfere with hydration and base pairing. By comparison, the shorter C16 chain attached to O2′ in the shallow and wide minor groove lacks opportunities to interfere with pairing and nucleobase stacking interactions. Even when the C28 chain manages to partially protrude from the major groove, it might assume orientations in the vicinity of the duplex backbones and interfere with phosphate and sugar hydration. Alternatively, it might obstruct metal ion binding. A better understanding of the conjugation site-specific effects of the length and saturation state of lipids on RNA duplex stability will require a more systematic investigation of a range of lipids in combination with thermodynamic experiments and 3D structure determination.

Ocular efficacy of GalNAc conjugated siRNAs

siRNA–GalNAc conjugates were designed to exploit recognition of the ASGPR to efficiently deliver dsRNAs to the liver [44]. These conjugates have been remarkably successful, resulting in several drugs that have a strongly favorable impact on the treatment of patients. ATTR is a relatively rare disease, with 5000–7000 cases diagnosed within the United States each year. Only a fraction of these patients report intraocular symptoms [17–20], so a simple path to the clinic that does not require extensive testing of a new compound might be the most viable.

Our data suggest that although inhibition of *TTR* expression can be achieved with GalNAc siRNA conjugates, potency, however, is low relative to lipid conjugates due to absence of ASGPR in eye. Our results suggest that the application of existing clinically proven siRNA drugs such as AMVUTTRA to target *TTR* expression is plausible and suggest thoughtful consideration related to optimizing ocular delivery, as their potency, and safety have already been established for hepatocyte delivery.

Comparing ocular efficacy of ASOs and siRNA

ASOs and siRNAs are mechanistically different approaches to gene silencing. Comparing the two approaches is not straightforward because a fair comparison would require independent development projects aimed at identifying the optimal siRNA and the optimal ASO respectively for a given target. Previously, we examined gapmer ASOs targeting *MALAT-1*, a nuclear noncoding RNA that is widely used as a surrogate for ASO target engagement [25, 29]. Comparing the data of our ASO and siRNA conjugate studies is difficult because the target genes are different. In addition, their mRNA transcripts are in different cellular compartments (*TTR* in cytoplasm, *MALAT-1* in the nucleus). IC_{50} values are approximations due to the relatively large error bars from measurements in tissues where *TTR* expression is low. Nevertheless, our past and present results are suggestive. We also note that Garanto and coworkers have demonstrated that a variety of different ASO chemistries can be active in the retina and can penetrate different layers of the retina [45].

The most potent anti-*TTR* conjugates used in our current study, TTRb–O2′–C16 and TTRb–C5–C28 have similar approximate IC_{50} values. Within the acknowledged limitations of the comparisons, ocular administration of siRNAs and ASOs appears to have similar potential for gene silencing. The anti-MALAT-1 ASO inhibited MALAT-1 with IC_{50} values of ∼0.5–1 μg/injection for each eye tissue. We have not had a chance to test TTR targeting ASOs yet but there are approved TTR ASOs (Tegsedi and WAINUVA) are available (1–3). It has also been reported that the duration of silencing is much longer for siRNAs they require less frequent dosing. Nevertheless, both RNAi and ASOs are viable platforms for development of nucleic acid therapeutics in the eye. Moving forward, inhibition by siRNAs or ASOs suggests that these modalities are the foundation for development paths toward the treatment of other ocular diseases, such as Fuchs' endothelial corneal dystrophy [46].

Conclusions

Ocular silencing of *TTR* expression demonstrates the potential of lipid-modified siRNAs to inhibit gene expression throughout diverse eye tissues. Inhibition can be achieved in both the anterior and posterior segments of the eye. While subsequent studies will be necessary to fully characterize and optimize both siRNA chemistry and injection routes of delivery, the inhibition of *TTR* that we observe suggests that the RNAi

approach will be a valuable option for therapeutic development programs that aim to use gene knock down strategies to alleviate diseases of the eye. Reducing the 2′-F content from TTRa to TTRb in siRNA will improve metabolic stability and changing major groove versus minor groove orientation of the conjugation ligand will impact biological potency. These were reflected in the divergent activities of the TTRa–C5–C16 and TTRb–O2′–C16 and TTRb–C5–C28 siRNA–lipid conjugates. This direct comparison of conjugation sites based biological outcome is an important result of this study. It is likely that more potent conjugates await discovery and that the eye will become an increasingly important target for nucleic acid therapeutics.

Acknowledgements

We are grateful to Tony Walshe and Sarah LeBlanc for their critical review of this manuscript.

Author contributions: Jiaxin Hu (Methodology, Investigation [equal]), Xin Gong (Methodology, Investigation [equal]), Jayanta Kundu (Methodology, Investigation), Dhrubajyoti Datta (Methodology, Investigation), Martin Egli (Conceptualization, Writing, Funding), Muthiah Manoharan (Conceptualization, Writing, Funding), V. Vinod Mootha (Conceptualization, Writing, Funding [equal]), David R. Corey (Conceptualization, Writing, Funding [equal])

Supplementary data

Supplementary data is available at NAR online.

Conflict of interest

M.M., J.K., and D.D. are employees of Alnylam Pharmaceuticals. V.V.M. is the Paul T. Stoffel/Centex Professor in Clinical Care. D.R.C. is the Rusty Kelley Professor of Biomedical Science. V.V.M., D.R.C., and J.H. hold a patent related to the use of dsRNAs to treat Fuch's endothelial corneal dystrophy. D.R.C. holds the position of Executive Editor for Nucleic Acids Research and has not peer reviewed or made any editorial decisions for this paper.

Funding

This study was supported by grants R01EY022161 (V.V.M.) and R35GM118103 (D.R.C.) from the National Institutes of Health, Bethesda, MD, a Challenge Grant from Research to Prevent Blindness (RPB), a Core Grant for Vision Research (P30EY030413), and the Welch Foundation (I-2184 to D.R.C.). Funding to pay the Open Access publication charges for this article was provided by National Institutes of Health.

Data availability

All data described are contained within the article and Supplementary data.

References

1. Egli M, Manoharan M. Chemistry, structure and function of approved oligonucleotide therapeutics. *Nucleic Acids Res* 2023;**51**:2529–73. https://doi.org/10.1093/nar/gkad067
2. Hofman CR, Corey DR. Targeting RNA with synthetic oligonucleotides: clinical success invites new challenges. *Cell Chemical Biology* 2024;**31**:125–38. https://doi.org/10.1016/j.chembiol.2023.09.005
3. Jadhav V, Vaishnaw A, Fitzgerald K. *et al.* RNA interference in the era of nucleic acid therapeutics. *Nat Biotechnol* 2024;**42**:394–405. https://doi.org/10.1038/s41587-023-02105-y
4. Nair JK, Willoughby JLS, Chan A. *et al.* Multivalent N-acetylgalactosamine-conjugated siRNA localizes in hepatocytes and elicits robust RNAi-mediated gene silencing. *J. Am. Chem. Soc.* 2014;**136**:16958–61. https://doi.org/10.1021/ja505986a
5. Khan T, Weber H, DiMuzio J. *et al.* Silencing myostatin using cholesterol-conjugated siRNAs induces muscle growth. *Molecular Therapy - Nucleic Acids* 2016;**5**:e342. https://doi.org/10.1038/mtna.2016.55
6. Engelbeen S, Pasteuning-Vuhman S, Boertje-van der Meulen J. *et al.* Efficient downregulation of Alk4 in skeletal muscle after systemic treatment with conjugated siRNAs in a mouse model for Duchenne muscular dystrophy. *Nucleic Acid Ther* 2023;**33**:26–34. https://doi.org/10.1089/nat.2022.0021
7. Malecova B, Burke RS, Cochran M. *et al.* Targeted tissue delivery of RNA therapeutics using antibody-oligonucleotide conjugates (AOCs). *Nucleic Acids Res* 2023;**51**:5901–10. https://doi.org/10.1093/nar/gkad415
8. Belgrad J, Tang Q, Hildebrand S. *et al.* A programmable dual-targeting siRNA scaffold supports potent two-gene modulation in the central nervous system. *Nucleic Acids Res* 2024;**52**:6099–113. https://doi.org/10.1093/nar/gkae368
9. Brown KM, Nair JK, Janas MM. *et al.* Expanding RNAi therapeutics to extrahepatic tissues with lipophilic conjugates. *Nat Biotechnol* 2022;**40**:1500–8. https://doi.org/10.1038/s41587-022-01334-x
10. Geary RS, Henry SP, Grillone LR. Fomivirsen. *Clin Pharmacokinet* 2002;**41**:255–60. https://doi.org/10.2165/00003088-200241040-00002
11. Zhou J, Rossi J. Aptamers as targeted therapeutics: current potential and challenges. *Nat Rev Drug Discov* 2017;**16**:181–202. https://doi.org/10.1038/nrd.2016.199
12. Hoy SM. Patisiran: first Global approval. *Drugs* 2018;**78**:1625–31. https://doi.org/10.1007/s40265-018-0983-6
13. Keam SJ. Vutrisiran: first approval. *Drugs* 2022;**82**:1419–25. https://doi.org/10.1007/s40265-022-01765-5
14. Adams D, Tournev IL, Taylor MS *et al.* Efficacy and safety of vutrisiran for patients with hereditary transthyretin-mediated amyloidosis with polyneuropathy: a randomized clinical trial. *Amyloid* 2023;**30**:18–26. https://doi.org/10.1080/13506129.2022.2091985
15. Coelho T, Marques W Jr, Dasgupta NR. *et al.* Eplontersen for hereditary transthyretin amyloidosis with polyneuropathy. *JAMA* 2023;**330**:1448–58. https://doi.org/10.1001/jama.2023.18688
16. Fontana M, Berk JL, Gillmore JD. *et al.* Vutrisiran in patients with transthyretin amyloidosis with cardiomyopathy. *N Engl J Med* 2025;**392**:33–44. https://doi.org/10.1056/NEJMoa2409134
17. Beirão JM, Malheiro J, Lemos C. *et al.* Ophthalmological manifestations in hereditary transthyretin (ATTR V30M) carriers: a review of 513 cases. *Amyloid* 2015;**22**:117–22. https://doi.org/10.3109/13506129.2015.1015678
18. Reynolds MM, Veverka KK, Gertz MA. *et al.* Ocular manifestations of familial transthyretin amyloidosis. *Am J Ophthalmol* 2017;**183**:156–62. https://doi.org/10.1016/j.ajo.2017.09.001
19. Cambieri C, Marenco M, Colasanti T. *et al.* Does Patisiran reduce ocular transthyretin synthesis? A pilot study of two cases. *CN* 2023;**21**:2543–9. https://doi.org/10.2174/1570159X21666230623094710
20. Ruiz-Medrano J, Puertas M, Almazán-Alonso E. *et al.* Ophthalmologic involvement in patients with hereditary transthyretin amyloidosis. *Retina* 2023;**43**:49–56. https://doi.org/10.1097/IAE.0000000000003641

21. O'Leary F, Campbell M. The blood-retina barrier in health and disease. *FEBS J* 2023;**290**:878–91. https://doi.org/10.1111/febs.16330
22. Ong DE, Davis JT, O'Day WT. *et al.* Synthesis and secretion of retinol-binding protein and transthyretin by cultured retinal pigment epithelium. *Biochemistry* 1994;**33**:1835–42. https://doi.org/10.1021/bi00173a029
23. Minnella AM, Rissotto R, Antoniazzi E. *et al.* Ocular Involvement in hereditary amyloidosis. *Genes* 2021;**12**:955. https://doi.org/10.3390/genes12070955
24. Ito T, Ueno Y, Komatsu Y. *et al.* Synthesis, thermal stability and resistance to enzymatic hydrolysis of the oligonucleotides containing 5-(N-aminohexyl)carbamoyl-2'-O-methyluridines. *Nucleic Acids Res* 2003;**31**:2514–23. https://doi.org/10.1093/nar/gkg374
25. Chau VQ, Hu J, Gong X. *et al.* Delivery of antisense oligonucleotides to the cornea. *Nucleic Acid Ther* 2020;**30**:207–14. https://doi.org/10.1089/nat.2019.0838
26. Wolfrum C, Shi S, Jayaprakash KN. *et al.* Mechanisms and optimization of in vivo delivery of lipophilic siRNAs. *Nat Biotechnol* 2007;**25**:1149–57. https://doi.org/10.1038/nbt1339
27. Datta D, Kumar P, Mandal S. *et al.* Conformation matters: siRNAs with antisense strands with 5′-(E)-vinyl-phosphonate-α-l-LNA elicit stronger RNAi-mediated gene silencing than those with 5′-(E)-vinyl-phosphonate-LNA. *Chem. Commun.* 2024;**60**:13024–7. https://doi.org/10.1039/D4CC04302B
28. Boulton M, Dayhaw-Barker P. The role of the retinal pigment epithelium: topographical variation and ageing changes. *Eye* 2001;**15**:384–9. https://doi.org/10.1038/eye.2001.141
29. Hu J, Gong X, Fan Y. *et al.* Modulation of gene expression in the eye with antisense oligonucleotides. *Nucleic Acid Ther* 2023;**33**:339–47. https://doi.org/10.1089/nat.2023.0044
30. Herbert J, Cavallaro T, Martone R. The distribution of retinol-binding protein and its mRNA in the rat eye. *Invest Ophthalmol Vis Sci* 1991;**32**:302–9.
31. Soutschek J, Akinc A, Bramlage B. *et al.* Therapeutic silencing of an endogenous gene by systemic administration of modified siRNAs. *Nature* 2004;**432**:173–8. https://doi.org/10.1038/nature03121
32. Cai Y, Lou C, Wengel J. *et al.* Albumin-binding fatty acid-modified gapmer antisense oligonucleotides for modulation of pharmacokinetics. *Methods Mol Biol* 2020;**2176**:163–74.
33. Fuchs H, Igney F. Binding to ocular albumin as a half-life extension principle for intravitreally injected drugs: evidence from mechanistic rat and Rabbit studies. *J Ocul Pharmacol Ther* 2017;**33**:115–22. https://doi.org/10.1089/jop.2016.0083
34. Tiwari R, Sethiya NK, Gulbake AS. *et al.* A review on albumin as a biomaterial for ocular drug delivery. *Int J Biol Macromol* 2021;**191**:591–9. https://doi.org/10.1016/j.ijbiomac.2021.09.112
35. Pomyalov S, Minetti CA, Remeta DP. *et al.* Structural and mechanistic insights into the transport of aristolochic acids and their active metabolites by human serum albumin. *J Biol Chem* 2024;**300**:107358. https://doi.org/10.1016/j.jbc.2024.107358
36. Pettersen EF, Goddard TD, Huang CC. *et al.* UCSF Chimera–a visualization system for exploratory research and analysis. *J Comput Chem* 2004;**25**:1605–12. https://doi.org/10.1002/jcc.20084
37. Li S, Olson WK, Lu X-J. Web 3DNA 2.0 for the analysis, visualization, and modeling of 3D nucleic acid structures. *Nucleic Acids Res* 2019;**47**:W26–34. https://doi.org/10.1093/nar/gkz394
38. Sheu-Gruttadauria J, Pawlica P, Klum SM. *et al.* Structural basis for target-directed MicroRNA degradation. *Mol Cell* 2019;**75**:1243–55. https://doi.org/10.1016/j.molcel.2019.06.019
39. van der Vusse GJ. Albumin as fatty acid transporter. *Drug Metab Pharmacokinet* 2009;**24**:300–7. https://doi.org/10.2133/dmpk.24.300
40. Ashbrook JD, Spector AA, Santos EC. *et al.* Long chain fatty acid binding to human plasma albumin. *J Biol Chem* 1975;**250**:2333–8. https://doi.org/10.1016/S0021-9258(19)41721-3
41. Manoharan M, Inamati GB, Lesnik EA. *et al.* Improving antisense oligonucleotide binding to human serum albumin: dramatic effect of ibuprofen conjugation. *ChemBioChem* 2002;**3**:1257–60. https://doi.org/10.1002/1439-7633(20021202)3:12%3C1257::aid-cbic1257%3E3.0.co;2-2
42. Lacroix A, Fakih HH, Sleiman HF. Detailed cellular assessment of albumin-bound oligonucleotides: increased stability and lower non-specific cell uptake. *J Controlled Release* 2020;**324**:34–46. https://doi.org/10.1016/j.jconrel.2020.04.020
43. Hoogenboezem EN, Patel SS, Lo JH. *et al.* Structural optimization of siRNA conjugates for albumin binding achieves effective MCL1-directed cancer therapy. *Nat Commun* 2024;**15**:1581. https://doi.org/10.1038/s41467-024-45609-0
44. Springer AD, Dowdy SF. GalNAc-siRNA conjugates: leading the way for delivery of RNAi therapeutics. *Nucleic Acid Ther* 2018;**28**:109–18. https://doi.org/10.1089/nat.2018.0736
45. Vázquez-Domínguez I, Anido AA, Duijkers L. *et al.* Efficacy, biodistribution and safety comparison of chemically modified antisense oligonucleotides in the retina. *Nucleic Acids Res* 2024;**52**:10447–63. https://doi.org/10.1093/nar/gkae686
46. Hu J, Shen X, Rigo F. *et al.* Duplex RNAs and ss-siRNAs block RNA foci associated with Fuchs' Endothelial corneal dystrophy. *Nucleic Acid Ther* 2019;**29**:73–81. https://doi.org/10.1089/nat.2018.0764

Received: March 7, 2025. **Revised:** April 25, 2025. **Editorial Decision:** April 25, 2025. **Accepted:** May 1, 2025